

Assessment of Propulsor On-Design and Off-Design Impacts on BLI Effects

Jai Ahuja* and Dimitri N. Mavris †

*Aerospace Systems Design Laboratory, School of Aerospace Engineering,
Georgia Institute of Technology, Atlanta, GA, 30332, USA*

As part of an effort to develop a parametric and coupled aero-propulsive conceptual design methodology for boundary layer ingesting (BLI) aircraft, there is a need to investigate propulsor sizing and off-design impacts on the ingested boundary layer. This study uses 3D CFD analysis to quantify the BLI effects trends as a function of fan annulus area and mass flow rate required, for engine locations similar to those on the the D8, NOVA-BLI and the STARC-ABL concepts. This study extends previous work that relied on CFD analysis of an axisymmetric model for the STARC-ABL concept. The results from this study highlight the propulsor’s contribution to the aero-propulsive coupling inherent in BLI concepts.

I. Nomenclature

Symbols and Acronyms

A	Area
BLI	Boundary layer ingestion
BPR	Bypass ratio
C_p	Pressure coefficient
$C_{P_{K_{in}}}$	Non dimensional $P_{K_{in}}$
d	Diameter
FPR	Fan pressure ratio
\dot{m}	Mass flow rate
M	Mach number
\hat{n}	Unit normal vector for a control volume boundary surface
OPR	Overall pressure ratio
p	Static pressure
P_K	Net mechanical power added to the flow by the propulsor
$P_{K_{in}}$	P_K evaluated at propulsor inlet
p_t	Total pressure
S_{ref}	Reference area for non-dimensional coefficients
T	Static temperature
T_t	Total temperature
\mathbf{V}	Velocity vector
V	Flow velocity magnitude

Engine Station Numbers (Subscripts)

∞	Freestream
1	Inlet highlight plane
2	Fan face
17	Bypass nozzle inlet plane
7	Core nozzle inlet plane
19	Bypass nozzle exit plane
9	Core nozzle exit plane

Greek

η_{PR}	Pressure recovery
μ	Dynamic viscosity
ρ	Static density
τ_w	Wall shear stress

*PhD Candidate, Aerospace Systems Design Laboratory, Georgia Institute of Technology, AIAA Student Member

†S.P. Langley Distinguished Regents Professor, Georgia Institute of Technology, AIAA Fellow

II. Introduction

Boundary layer ingesting propulsors are considered a promising technology to minimize aircraft fuel burn. Modeling the changes in propulsive power requirements due to BLI (i.e. the BLI effects) at the conceptual design stage necessitates a parametric approach, given that both the propulsor [1–3] and airframe design [4] affect the ingested flow properties. As such, a point design estimate of the impacts of BLI on vehicle performance fails to capture the aero-propulsive coupling that is inherent in BLI concepts. Previous work by the author has focused on quantifying the role played by the airframe design on the BLI effects [4], and also touched on the propulsor influence [5]. However, the latter research relied on CFD analysis of a 2D axisymmetric STARC-ABL model. The present effort expands on previous work by focusing on concepts with engine locations similar to the D8, NOVA-BLI and the STARC-ABL. 3D CFD analysis is used to quantify the impact of the propulsor on-design and off-design characteristics on the ingested airflow, and determine whether the engine location affects the trends. The results from this study aid development of a coupled aero-propulsive design methodology for BLI concepts that is discussed in [6].

III. Background

The discussion in this section establishes the necessity of capturing variations in the ingested boundary layer properties as a function of propulsor fan size (on-design) and flow rate requirements (off-design). At a high level, changes in engine cycle design parameters and operation are related to the physical impacts on the ingested flow. Quantifying the sensitivity of the BLI effects, formally defined in section IV, to the propulsor establishes the extent of the engine’s contribution to the aero-propulsive coupling and thus to the overall vehicle design and performance. The experiments presented in this paper shed light on the sensitivities. Observed trends in the BLI effects, presented in sections VI and VII, are related to the physics discussed in this section and extended in section V.

Consider the propulsor schematic shown in Fig. 1. This figure is representative of BLI propulsors on the D8 and NOVA-BLI concepts. For configurations like the STARC-ABL, where the BLI propulsor is an electrically driven ducted fan, the core is absent and only the fan is modeled. The specific flow rate through the fan, i.e., mass flow rate per

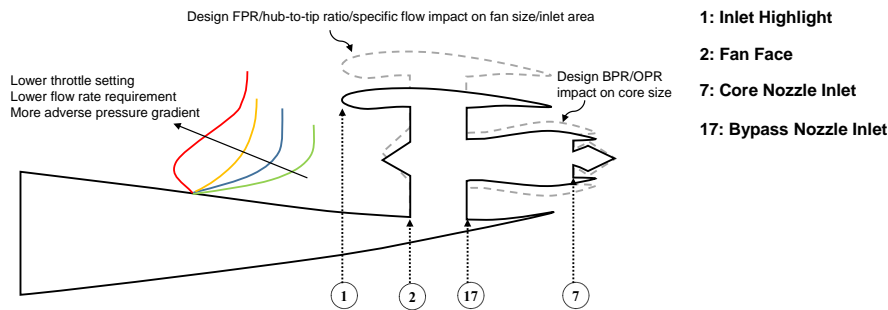


Fig. 1 BLI propulsor schematic

unit area, is a measure of how much air flow can be sucked in by the fan for a given annulus area. This metric, in engine on-design, is a measure of blade design technology, and is typically assumed at the conceptual design stage given current fan technology availability, or future technology readiness levels. In engine on-design, for both ducted fans and separate flow turbofans, given a design FPR, assumed specific flow, and specified hub to tip ratio, the size of the fan is determined by the mass flow requirements at the most critical engine sizing point, typically top of climb. Thus, the annulus area at station 2 and as a consequence stations 1 and 17 in Fig. 1, are a fallout of the chosen design parameters and fan technology assumption. For a given thrust requirement, assumed specific flow, and hub to tip ratio, a decrease in design FPR increases the fan diameter required to allow for higher mass flow. Similarly, a decrease in the assumed specific flow, for the same requirements, results in a larger fan. For turbofan engines, size of the core is determined by the design OPR, assumed core specific flow, and the design BPR. For a given BPR and assumed core specific flow, as design OPR decreases, the core size increases to allow the same mass flow. For a fixed FPR, assumed core specific flow, and OPR, decreasing BPR increases the flow rate requirement for the core, and thus the core size increases.

For a given mass flow rate, an increase in fan annulus area reduces the average inflow velocity and increases static pressure, while a decrease in size has the opposite effect, due to conservation of mass and momentum. The impact

of fan size on the shapes of the ingested boundary layer profiles is evident from Gray’s studies [1]. The fan size also affects the captured streamtube, impacting the amount of boundary layer flow ingested relative to clean flow. Total pressure is typically higher in the freestream than in the boundary layer. Ingesting a larger percentage of clean flow by increasing the fan size has a favorable impact on the averaged total pressure seen by the fan. This benefit of course is counteracted by the added penalties of larger nacelle wetted area and weight. This trade-off seems to suggest that there is an optimum fan size that maximizes the BLI benefits, while minimizing the adverse impacts on performance. Significant variations in the BLI effects due to changes in fan size places greater emphasis on the optimal selection of engine variables like fan hub to tip ratio and design FPR for example, relative to conventional podded engine design. These variables influence the BLI effects through their impact on fan size, which in turn affects the fuel requirements and thus airframe sizing for a given mission. Unlike conventional aircraft with podded engines, where these design parameters can be set independently from the airframe, for embedded engine concepts where the BLI effects show significant sensitivity to fan size, this decoupled approach is no longer feasible.

With regards to engine size, it can be reasonably assumed that the BLI effects calculated from the ingested boundary layer are *directly* dependent only on the fan size, and not the core size. While cycle design parameters like OPR, BPR, and turbine inlet temperature for example have a direct impact on the vehicle fuel burn, these parameters only have an *indirect* influence on the ingested boundary layer properties. As the compressor and turbine design changes, the fan size and operation changes accordingly, for the same design requirements. Thus, the influence on the BLI effects due to changes in the on-design characteristics of the core are felt through the corresponding changes in the fan design.

In engine off-design, the throttle setting is adjusted such that engine thrust matches the vehicle drag at a given point in the mission. For turbofans, this entails varying the fuel flow rate, which then adjusts the shaft speed. FPR and OPR in off-design are a fallout of the shaft speed and turbomachinery performance maps, and the flow rate needed to match engine thrust with vehicle drag, for the sized engine, is thus determined. Thermodynamic properties at stations 17 and 7 are also a fallout. For electrically driven ducted fans like on the STARC-ABL, varying throttle amounts to changing the input shaft power, with the flow rate requirements, FPR, and fan exit conditions varying as a function of shaft power. The impact of the propulsor operation, i.e., mass flow rate requirements, on the boundary layer can be explained using standard boundary layer theory. The ingested boundary layer properties are largely dependent on the externally imposed streamwise pressure gradient. While the airframe contour entering the propulsor influences the external inviscid stream, thus affecting the pressure gradient imposed on the boundary layer, the propulsor throttle setting, i.e., amount of airflow being sucked in, also impacts this pressure gradient. Fig. 1 shows the impact of varying pressure gradient on the boundary layer profiles. Positive (adverse) pressure gradients slow down the flow. The velocity gradient at the wall, $\left. \frac{du}{dy} \right|_w$, decreases as the pressure gradient becomes more adverse, and thus the wall shear stress, $\tau_w = \mu \left. \frac{du}{dy} \right|_w$, decreases. If the pressure gradient is too adverse, the flow will separate as depicted by the red profile in Fig. 1, leading to reversed flow and significant losses in total pressure in that region. This separation bubble displaces neighboring streamlines, altering the effective shape of the airframe, thus impacting the ingested streamtube. As a reminder, changes to flow rate are not the only cause for variations in the pressure gradient. As discussed above, changes to the fan size, for a given flow rate, also affect pressure. In addition to influencing the pressure gradient and wall shear, changes to the required mass flow rate, for a given inlet area, also affect the extent of the captured streamtube, due to mass conservation. Sensitivity of the BLI effects to engine mass flow rate also affects fuel weight requirements given variations in engine fuel burn at different points in the mission profile. Thus, engine throttle impacts on the BLI effects need to be investigated.

IV. Methodology

A. Definition of BLI Effects

The power balance aircraft performance bookkeeping proposed by Drela [7] is adopted for this study as a means to sidestep the thrust-drag bookkeeping ambiguity for BLI concepts. Based on the work by Drela and Hall [8], a derivation of the BLI effects, and how power balance relates to the conventional thrust-drag bookkeeping was presented in [4]. For this study, the BLI effects of interest are the mechanical energy defect of the ingested boundary layer, i.e., $P_{K_{in}}$, defined by the following equation:

$$P_{K_{in}} = \iint - \left[(p - p_{\infty}) + \frac{1}{2} \rho (V^2 - V_{\infty}^2) \right] \mathbf{v} \cdot \hat{\mathbf{n}} dA \quad (1)$$

which is then non-dimensionalized by $\frac{1}{2}\rho_\infty V_\infty^3 S_{\text{ref}}$, and pressure recovery η_{PR} , which is given by:

$$\eta_{PR} = \frac{p_{t_2}}{p_{t_1}} \frac{p_{t_1}}{p_{t_\infty}} = \frac{p_{t_2}}{p_{t_\infty}} \quad (2)$$

This definition of pressure recovery accounts for total pressure losses in the boundary layer over the airframe surface and within the inlet.

B. Description of Experiments

Two types of propulsor locations are considered for this study based on the circumferential extent of ingested distorted flow. For both the D8 and the NOVA BLI, the ingested distortion extent is similar to that shown in Fig. 2a, even though the position and orientation of the engine relative to the fuselage is different between the concepts. Here, the lower portion of the fan ingests the airframe boundary layer, in addition to the boundary layer formed on the nacelle wall and spinner. While the side mounted engine geometry is used in experiment 1, it is expected that the trends observed are also similar for a top mounted engine like on the D8. In experiment 2, a fuselage trailing edge mounted propulsor like on the STARC-ABL is considered. As shown in Fig. 2b, the entire circumferential distortion extent on the fan annulus is primarily due to the airframe boundary layer (excluding the nacelle wall boundary layer). The objective behind considering these two distinct cases is to assess whether the trends observed for one are consistent with the other, or whether the extent of ingested distortion plays a role in affecting the sensitivities. The fuselage geometries used in experiment 1 and 2 are sized similar to the 737-8 in the 150-180 pax class. All experiments are conducted at the cruise condition of $M_\infty = 0.8$, altitude = 35,000ft, at a 0° angle of attack. The BLI effects, $C_{P_{K_{in}}}$ (non-dimensional $P_{K_{in}}$) and η_{PR} , are evaluated at both the fan face and the inlet highlight plane such that contributions from the airframe and nacelle can be isolated. The reference area S_{ref} is set to 1.

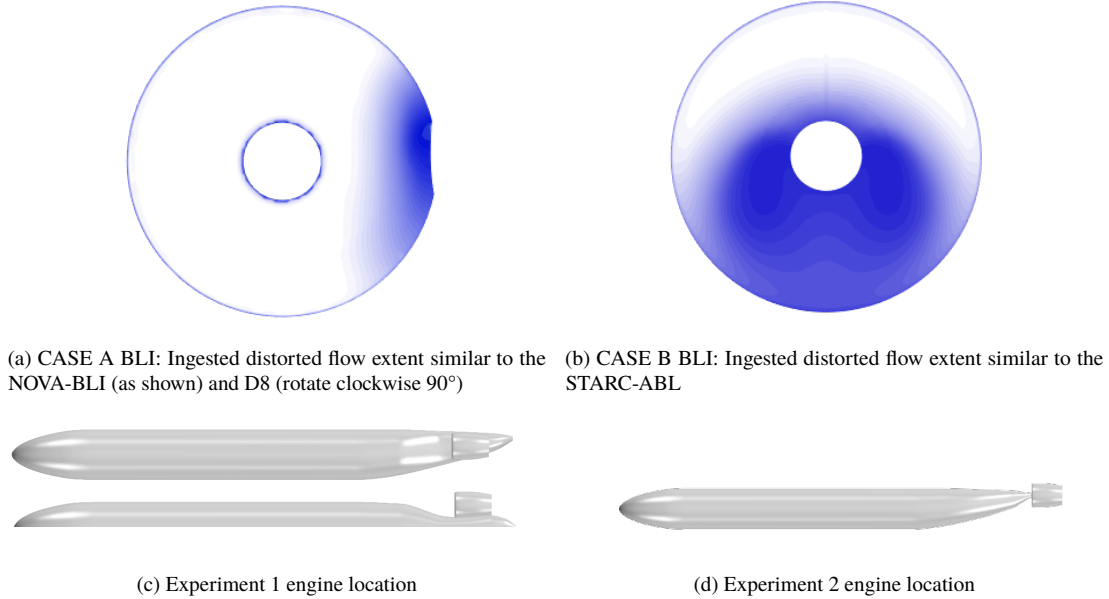


Fig. 2 Engine locations considered for experiments 1 and 2 based on extent of ingested distortion

1. Experiment 1

In this set of experiments, the engine is mounted to the side of the airframe, as shown in Fig. 2c. A structured design of experiments is created, where the same sweep in mass flow rate is considered for three fan diameters. A variation in fan diameter accounts for engine on-design impacts on the BLI effects. A change in mass flow rate required, for a fixed fan diameter, accounts for throttle effects in engine off-design conditions. An overview of the cases run is presented in Table 1.

Table 1 Experiments 1 and 2: Overview of Cases

Experiment	d_2 (in)	A_2 (ft ²)	Target \dot{m}_2 (lbm/s)	Experiment	d_2 (in)	A_2 (ft ²)	Target \dot{m}_2 (lbm/s)
1.1	69.9	24.97	452	2.1	69.9	24.97	348
1.2	69.9	24.97	434	2.2	69.9	24.97	321
1.3	69.9	24.97	393	2.3	77	30.32	422
1.4	77	30.32	466	2.4	77	30.32	374
1.5	77	30.32	452	2.5	77	30.32	348
1.6	77	30.32	434	2.6	77	30.32	321
1.7	77	30.32	393	2.7	85	36.94	537
1.8	85	36.94	466	2.8	85	36.94	502
1.9	85	36.94	452	2.9	85	36.94	422
1.10	85	36.94	434				
1.11	85	36.94	393				

As part of this propulsor size and operation exploration study, a wide enough, yet reasonable range is considered for the fan diameter and flow rate. The smallest fan size is similar to LEAP-1B engines on the Boeing 737-8. The largest fan diameter of is modeled off the NOVA-BLI [9]. The 77 in. fan diameter is considered as a center point case. Note that the fan sizes proposed for the D8, at 72 in. [10], and the STARC-ABL at 81 in. [11] are within this range. The required mass flow rates are obtained from the powerhooks generated by NPSS for a reference propulsor model, shown in Fig. 3, with the selected points shown using filled markers. The numbers above the points represent the power code corresponding to that operating point, and are included for reference. These flow rates cover potential points that are expected to be encountered in typical cruise conditions, with a small buffer. Low throttle and flight idle settings are ignored since insufficient power is produced for cruise.

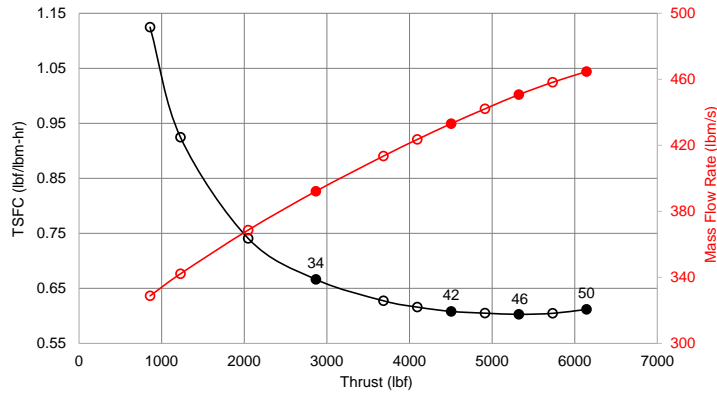


Fig. 3 Powerhook for the smallest propulsor at cruise conditions

2. Experiment 2

The objective of this set of trials is to determine how the trends observed in the previous experiments translate to the case where more boundary layer is ingested. The propulsor in this experiment is placed at the fuselage trailing edge, like on the STARC-ABL, as shown in Fig. 2d. The same fan annulus areas (A_2) are used as before, but the range on flow rate (\dot{m}_2) is increased. For $A_2 = 30\text{ft}^2$ and $A_2 = 37\text{ft}^2$, the upper bound is defined by when shocks appear in the inlet, while the lower bound is defined by the smallest mass flow that is possible without reversed flow at the fan face. The cases considered are shown in Table. 1. Given that there is only one common \dot{m}_2 point between the $A_2 = 30\text{ft}^2$ and $A_2 = 37\text{ft}^2$ propulsors, the trials for $A_2 = 25\text{ft}^2$ are conducted to augment data for A_2 trends.

C. CFD Model Setup

The commercially available CFD software STAR-CCM+ is used for mesh generation and solving the RANS equations. Steady state conditions and standard atmosphere properties are assumed. Symmetry about the x - z plane allows for half the domain to be modeled. The SST k - ω model is used for turbulence modeling. The propulsor is modeled with uniform powered boundary conditions. The fan face is modeled as a pressure outlet, while the bypass nozzle inlet is modeled as a stagnation inlet. The throttle setting is modeled in CFD as a variation in p_2 , p_{t17} and T_{t17} . To match the flow rate requirement for the engine predicted by the cycle code with that measured in CFD, p_2 in CFD is adjusted. In this study, the flow downstream of the fan is of no interest because metrics like fan exit mass flow, or net axial force for example are not being computed in CFD. The BLI effects are only dependent on the ingested flow, which does not depend on the geometry and boundary conditions downstream of the fan face *in the CFD domain*. Thus, the core and plug geometries can be excluded from the CFD model of the propulsor, thereby eliminating the need to carefully design these components, while also reducing the mesh size and overall computational expense.

An unstructured Cartesian mesh is used, with prism layers to capture the boundary layer. The near wall spacing is calculated such that a wall $y^+ \leq 1$ is achieved over the entire surface. A mesh sensitivity study is conducted to find an appropriately sized grid for the experiments. The aircraft configuration tested in experiment 1, with the smallest propulsor, is used for this grid refinement study. The optimal mesh settings found from this study are used for all cases in experiments 1 and 2. The boundary conditions at the fan face and exit are kept the same for each mesh refinement level. The BLI effects and mass flow rate measured at the fan face are tracked across the cases. Results for $C_{PK_{in}}$ and η_{PR} are shown in Fig. 4a, and for \dot{m}_2 in Fig. 4b. The final mesh chosen is indicated by a filled marker, and contains approximately 6 million cells.

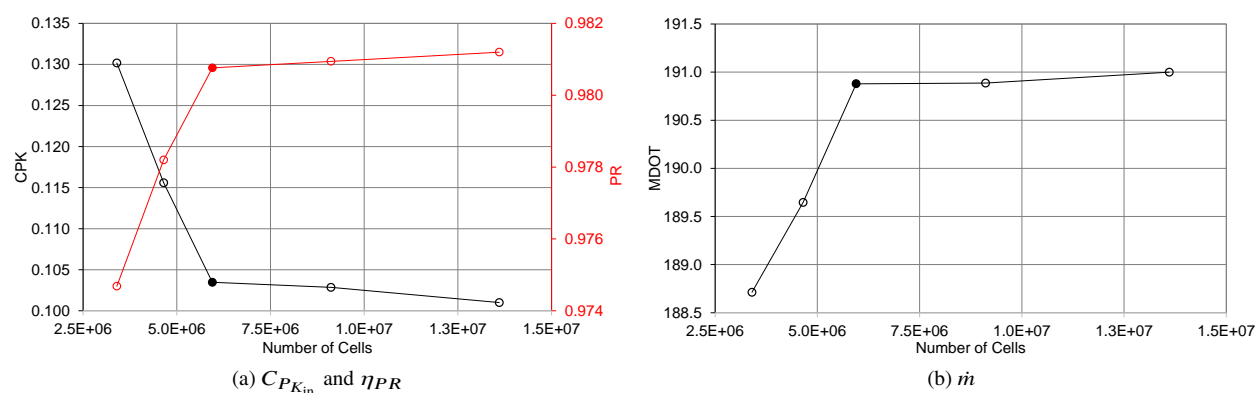


Fig. 4 Summary of results from mesh sensitivity trials

V. Expected Variations in BLI Effects

Now that the BLI effects have been formally defined, the discussion in section III can be tailored towards understanding how the BLI effects are expected to vary with fan annulus area (A_2) and flow rate (\dot{m}_2). This preliminary analysis helps support results obtained from the experiments, while also allowing one to easily identify exceptions or unexpected behavior that warrant further examination.

A. Trends in η_{PR}

Pressure recovery quantifies total pressure losses in the ingested flow. An increase in wall shear stress, or sources of high vorticity like shocks or recirculating flow in separation bubbles, result in a loss in total pressure and thus η_{PR} . The total pressure in the flow increases moving further away from the wall and is thus lower in the boundary layer than in the freestream, assuming no shocks. Since an increase in flow rate, for a given fan annulus area, increases the wall shear as discussed before, it can be hypothesized that η_{PR} negatively correlates with \dot{m} , assuming no flow separation at the measurement plane at which this metric is evaluated. With A_2 , for a fixed \dot{m} requirement, given that a larger propulsor ingests a bigger fraction of flow at a high total pressure, and that the inflow velocity is slower (lower wall shear stress), the averaged total pressure is expected to be higher. Thus, it is expected that η_{PR} shows a positive correlation with A_2 .

B. Trends in $C_{P_{K_{in}}}$

To understand how $C_{P_{K_{in}}}$ behaves, it is instructive to consider the two contributing sources to $C_{P_{K_{in}}}$. Eq. (1) is first divided by $\frac{1}{2}\rho_{\infty}V_{\infty}^3S_{ref}$ to non-dimensionalize the quantity, The resulting expression is then manipulated to a more convenient form to obtain the following at a given measurement station i :

$$C_{P_{K_{in}}} = \iint \left[\frac{\rho_i V_i}{\rho_{\infty} V_{\infty}} \left(1 - \frac{V_i^2}{V_{\infty}^2} \right) - C_{P_i} \frac{V_i}{V_{\infty}} \right] \frac{dS_i}{S_{ref}} \quad (3)$$

This metric quantifies the ingested kinetic energy thickness and the pressure-velocity component of the ingested flow. The measurement station i at which this integral is evaluated is 1 for the inlet highlight or 2 for the fan face. The $C_{P_{K_{in}}}$ integrand has the form of a polynomial as follows:

$$Qx(1 - x^2) - Rx \quad \text{where } x \equiv \frac{V_i}{V_{\infty}}; \quad Q \equiv \frac{\rho_i}{\rho_{\infty}} = f(x) \quad \text{and} \quad R \equiv C_{P_i} \quad (4)$$

Eq. (4) is a non-monotonic function in the domain $0 \leq x \leq C$ where C is a value typically $O(10^{-1})$. This function is shown notionally in Fig. 5.

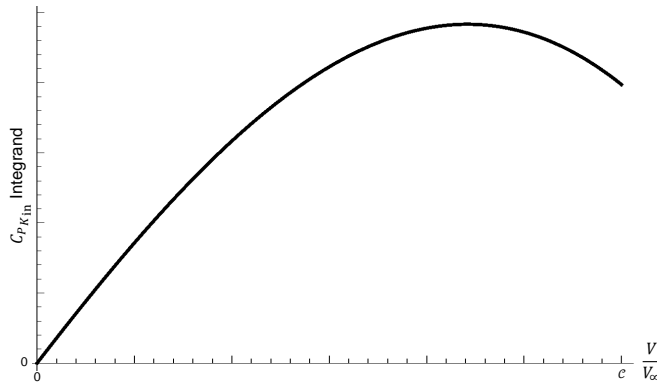


Fig. 5 Notional plot showing how the integrand of $C_{P_{K_{in}}}$ varies with $\frac{V_i}{V_{\infty}}$

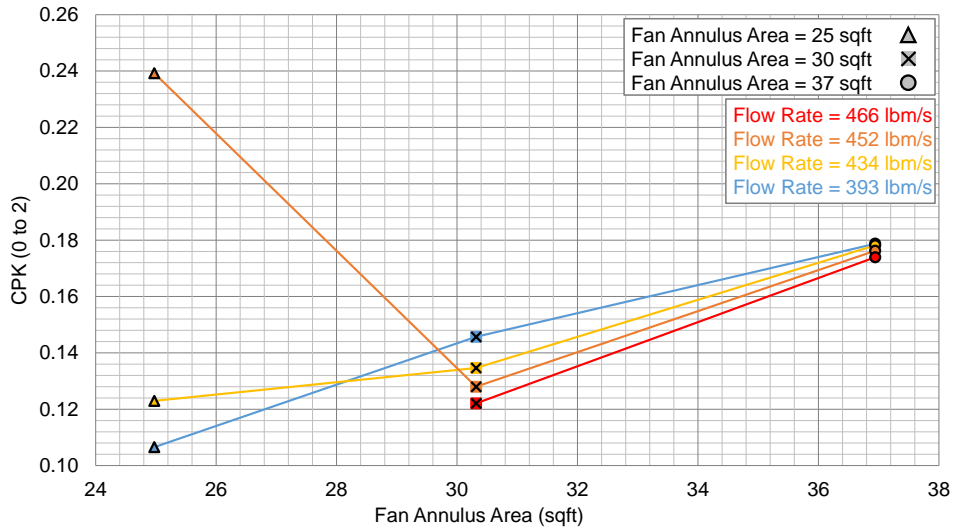
Low values of x correspond to points closer to a wall, within the ingested boundary layer, while higher values of x are typically found away from a wall. The highest velocity ratio at some point on the integration surface can be $O(1)$ outside the ingested boundary layer, for very high required \dot{m} . Note that for a uniform boundary condition propulsor model in CFD, the pressure coefficient (C_{P_2}) is at the same value at all points on the fan annulus, for a given \dot{m} . How $C_{P_{K_{in}}}$ varies depends on the rate at which the ingested KE-thickness changes with \dot{m} and A_2 , relative to the pressure-velocity component. Given that the ingested KE-thickness component is proportional to $\left(\frac{V_i}{V_{\infty}}\right)^3$ (not including the density dependence on velocity), it is expected that this term dominates in most instances. Pressure effects would have a stronger influence on $C_{P_{K_{in}}}$ trends for very low or very high \dot{m} , where flow separation or shocks are likely to occur in the ingested streamtube.

If there is significant BLI with a large portion of the boundary layer falling within the linear region of Fig. 5, then it can be hypothesized based on the functional form of $C_{P_{K_{in}}}$, the hypothesized significance of the ingested KE-thickness component, and the correlations of pressure, velocity, and mass flux (ρV) with \dot{m} , that an increase in \dot{m} will result in an increase in $C_{P_{K_{in}}}$. However, if the ingested boundary layer covers only a small fraction of the integration plane, then most of the integration plane sees a relatively higher $\frac{V_i}{V_{\infty}}$. Given the higher order effects of velocity on $C_{P_{K_{in}}}$, it is expected that for cases with low BLI, an increase in \dot{m} will result in a decrease in $C_{P_{K_{in}}}$, driven by the decrease in the ingested KE-thickness component. With respect to A_2 , for a given \dot{m} , an increase in A_2 is expected to shift most points on the integration area further to the left in Fig. 5, from conservation of mass, which is expected to have a favorable impact on the KE-thickness and thus $C_{P_{K_{in}}}$.

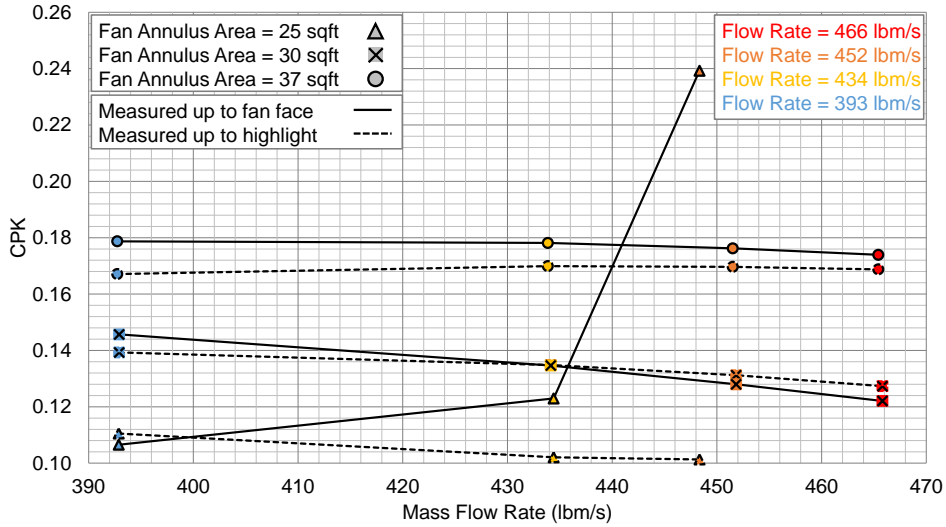
VI. Experiment 1: Case A Boundary Layer Ingestion

A. Variation of $C_{P_{K_{in}}}$ with A_2 and \dot{m}_2

Fig. 6a shows how $C_{P_{K_{in}}}$, measured at the fan face, varies as a function of the fan annulus area A_2 for a constant \dot{m}_2 requirement. The \dot{m}_2 curves are colored blue to red indicating different values of the flow rate. The same data are plotted in Fig. 6b to clearly illustrate how $C_{P_{K_{in}}}$ trends with \dot{m}_2 for a fixed A_2 . In this figure, different marker shapes are used to denote the three propulsor sizes considered. Solid lines denote trends for $C_{P_{K_{in}}}$ measured at the fan face, while dashed lines represent trends of $C_{P_{K_{in}}}$ measured at a plane slightly offset from the inlet highlight (not shown in Fig. 6a). The latter results quantify the airframe contribution to $C_{P_{K_{in}}}$ and how that varies with propulsor operation. The difference between the solid and dashed curves indicates the effective contribution of the inlet to $C_{P_{K_{in}}}$. In general, $C_{P_{K_{in}}}$ exhibits a positive correlation with respect to A_2 and negative with \dot{m}_2 , as hypothesized, with two exceptions where shocks are seen in the inlet, which will be discussed shortly.



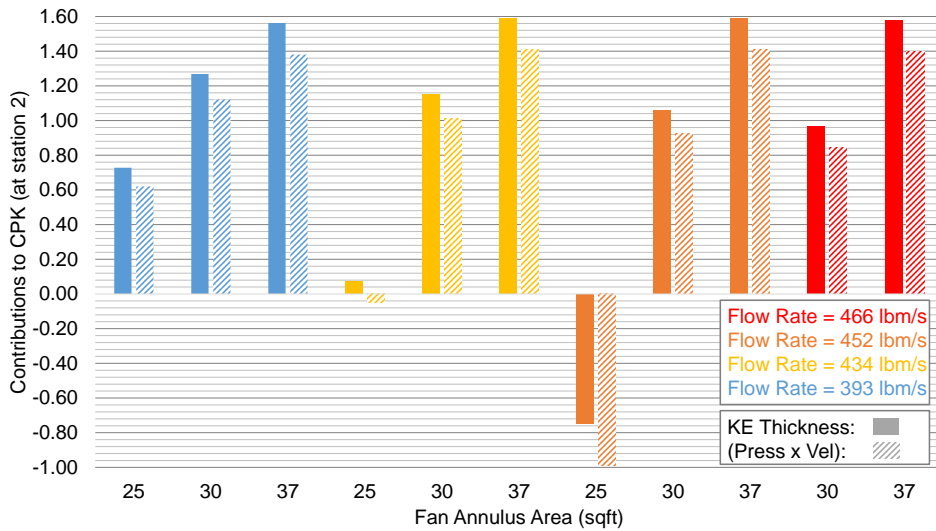
(a) $C_{P_{K_{in}}}$ variation with A_2 for different \dot{m}_2



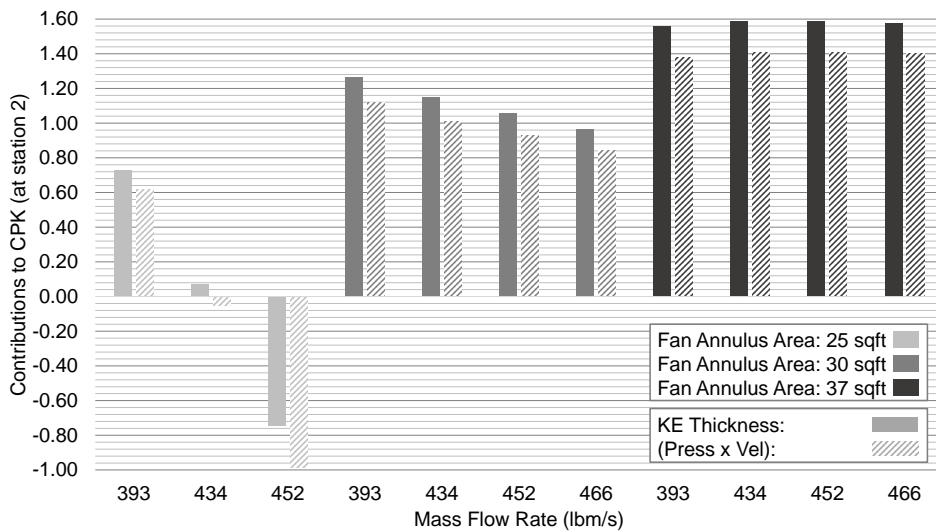
(b) $C_{P_{K_{in}}}$ variation with \dot{m}_2 for different A_2

Fig. 6 Experiment 1: variation of $C_{P_{K_{in}}}$ as a function of A_2 and \dot{m}_2

The contributions to $C_{P_{K_{in}}}$ are plotted in Figs. 7a and 7b corresponding to the perspectives shown in Figs. 6a and 6b respectively. Solid bars are used to represent the KE-thickness component, while hatched bars denote the pressure-velocity contribution. The net result is a subtraction of the pressure-velocity contribution from the KE-thickness as shown in Eq. (3). As the fan size increases, for a given \dot{m}_2 requirement, the ingested KE-thickness component increases given that the inflow velocity reduces, and thus the difference between the ingested velocity and freestream increases. There is a negative correlation between static pressure and velocity such that $C_{p_i} = \frac{p_i - p_\infty}{\frac{1}{2}\rho_\infty V_\infty^2}$ in Eq. (3) increases with a decrease in inflow velocity. Note, for most cases, the static pressure at the fan face is higher than ambient ($p_2 > p_\infty$). Thus, C_{p_i} is usually positive and $C_{p_i} \frac{V_i}{V_\infty}$ offsets the kinetic energy defect component when subtracted from it in Eq. (3). But, as C_{p_i} increases, the value of $\frac{V_i}{V_\infty}$ decreases such that the rate of increase in $C_{p_i} \frac{V_i}{V_\infty}$ is smaller than the rate of increase in the KE-thickness component. Given the dominance of the latter term, the net effect is an increase in



(a) Kinetic energy thickness and pressure-velocity contributions to $C_{P_{K_{in}}}$ varying with A_2 for different \dot{m}_2



(b) Kinetic energy thickness and pressure-velocity contributions to $C_{P_{K_{in}}}$ varying with \dot{m}_2 for different A_2

Fig. 7 Experiment 1: variation of kinetic energy thickness and pressure-velocity contributions to $C_{P_{K_{in}}}$ as a function of A_2 and \dot{m}_2 . The net result is a subtraction of the pressure velocity from the kinetic energy thickness component

$C_{P_{K_{in}}}$ with A_2 as hypothesized. Similar reasoning that relates changes in C_{P_i} and KE-thickness to $\frac{V_i}{V_\infty}$ can be applied to explain the trends with \dot{m}_2 , recognizing that the average velocity ratio must increase with \dot{m}_2 , for a fixed A_2 .

Fig. 8 shows how the KE-thickness *integrand* in Eq. (3) varies as a function of *average* ingested velocity ratio $\frac{V_i}{V_\infty}$. Moving right on the x axis thus corresponds to an increase in \dot{m}_2 or a decrease in A_2 . The average velocity ratio is computed for each of the CFD cases at cruise and these points are overlaid on this curve. Note the three distinct clusters of points, corresponding to the three propulsor sizes investigated. The distribution of points within these clusters, based on the value of \dot{m}_2 they correspond to, and the relative location of these clusters to each other on the curve, matches the KE-thickness trends seen in Fig. 7.

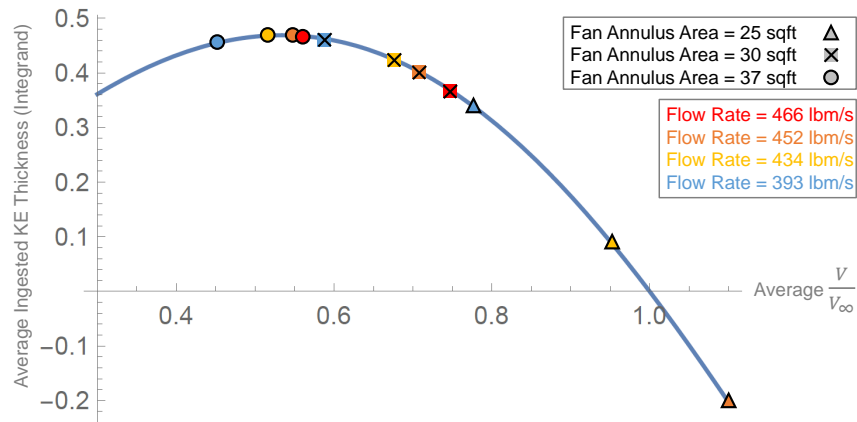


Fig. 8 Experiment 1: variation of average ingested kinetic energy thickness (integrand in Eq. (3)) with average ingested velocity ratio, measured at the fan face

The observation concerning the sensitivity of $C_{P_{K_{in}}}$ to \dot{m}_2 being dependent on the fan size, evident from Fig. 6, warrants further examination. This observation can be explained by comparing the streamtube captured by two propulsors of different sizes, shown in Fig. 9. In this top-view of the propulsor-airframe geometry, the outlines of the streamtubes captured by the 30ft² and 37ft² propulsors are traced for the smallest and largest mass flow rate tested. For a given inlet capture area, the streamtube capture area increases with \dot{m}_2 . However, in the region in front of the inlet

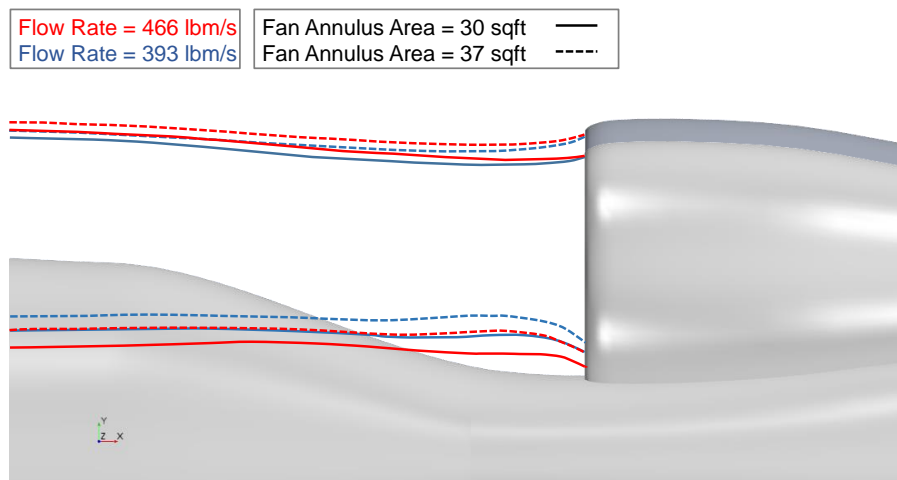


Fig. 9 Experiment 1: comparison of captured streamtubes for two propulsor sizes and mass flow rates (top view). This figure is a 2D view of the 3D ingested streamtube. The lower outline of the streamtubes shown vary in z direction out of the page

highlight, the streamtube captured by the larger propulsor is further away from the wall, than it is for the smaller one. Since the gradients in the ingested flow are larger closer to the wall, variations in streamtube capture area due to \dot{m}_2 have a more pronounced impact on $C_{P_{K_{in}}}$ for the smaller propulsor. In the region between the ingested streamtube and the fuselage wall, there is a separation bubble. Though not present in all cases, the extent of this recirculating flow grows with propulsor size and with a decrease in \dot{m}_2 , i.e, with a more adverse pressure gradient. This recirculating flow is not ingested by the fan for any of the cases tested, but rather, is spilled around the nacelle, as shown in Fig. 10.

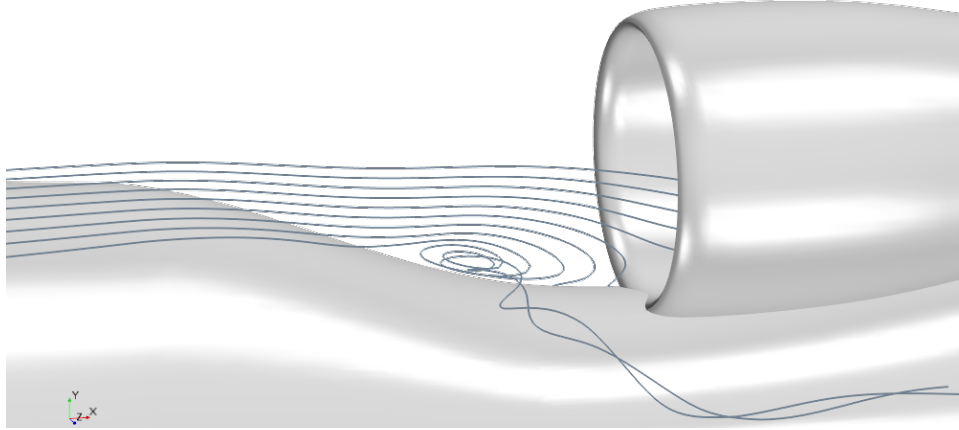


Fig. 10 Experiment 1: region of recirculating flow in front of inlet highlight, shown for $A_2 = 30\text{ft}^2$ and $\dot{m}_2 = 393\text{lbm/s}$

The two outliers to the trends discussed above are for the $A_2 = 25\text{ft}^2$ propulsor, with a required flow rate of $\dot{m}_2 = 452\text{lbm/s}$ and 434lbm/s . Due to BLI blockage effects, the flow rate required is too high for the given propulsor size, nacelle geometry, and propulsor location. As a consequence of this small area, large flow rate requirement, large portions of the fan face experience high Mach number flow, as seen in the sub figures on the right in Fig. 11. For $\dot{m}_2 = 452\text{lbm/s}$, the average fan face Mach number is higher than freestream, while for $\dot{m}_2 = 434\text{lbm/s}$, it is just below freestream. The corresponding static pressures at the fan face are below freestream, unlike the other cases tested. In addition, high flow Mach number around the nacelle lip and throat results in a shock just aft of the throat, which is stronger for $\dot{m}_2 = 452\text{lbm/s}$. As a result, the nacelle wall boundary layer thickens behind this shock. The influence of

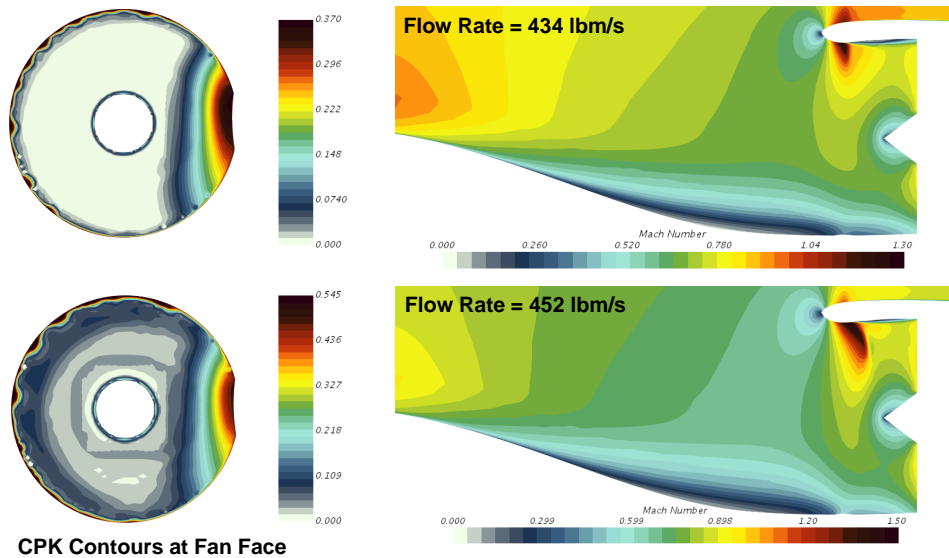
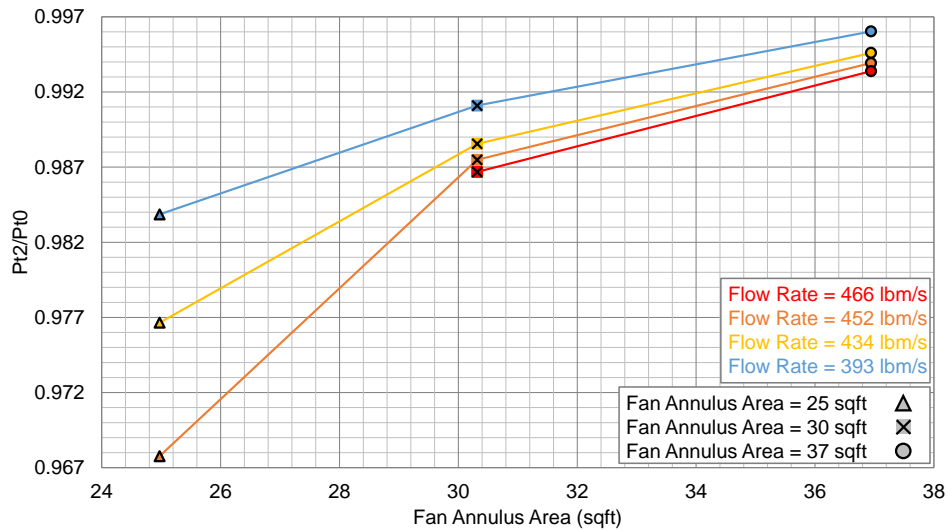


Fig. 11 Comparison of fan face $C_{P_{K_{in}}}$ contours and Mach contours for $A_2 = 25\text{ft}^2$ at two different mass flow rates

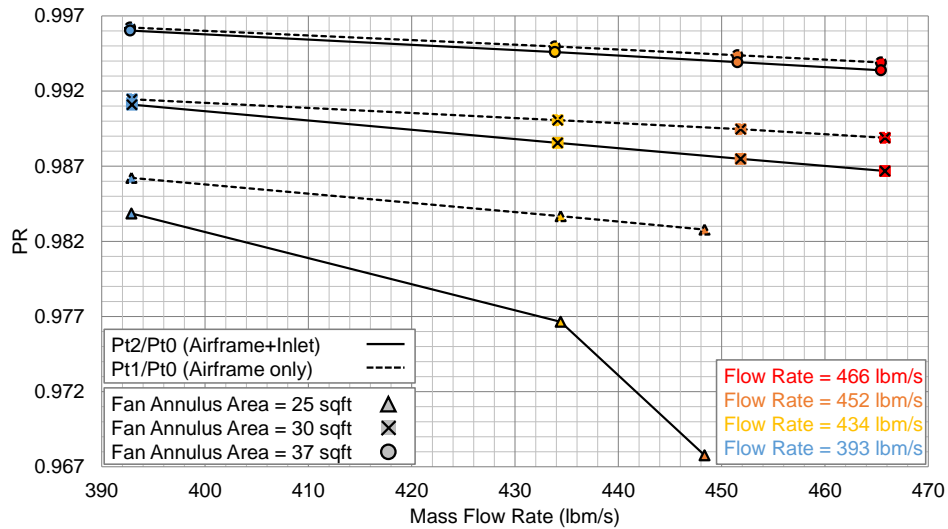
these aspects can be seen through the $C_{P_{K_{in}}}$ contours at the fan face in the sub figures on the left in Fig. 11. As a result of the higher than freestream fan face velocity, the kinetic energy thickness component is negative for $\dot{m}_2 = 452\text{lbm/s}$. The same is true for the pressure-velocity component due to the lower than freestream static pressure. But the magnitude of the latter term is much larger than the former, as seen in Fig. 7a, which has a favorable impact on $C_{P_{K_{in}}}$. The thicker nacelle wall boundary layer after the shock also has a beneficial contribution to $C_{P_{K_{in}}}$. These two effects combined account for the sharp increase in $C_{P_{K_{in}}}$ seen for the smallest fan at $\dot{m}_2 = 452\text{lbm/s}$. For $\dot{m}_2 = 434\text{lbm/s}$, the impact on $C_{P_{K_{in}}}$ is less significant than $\dot{m}_2 = 452\text{lbm/s}$, but still larger than for $\dot{m}_2 = 393\text{lbm/s}$ for $A_2 = 25\text{ft}^2$, which is a shock free case. Note, the case $\dot{m}_2 = 466\text{lbm/s}$ diverged for $A_2 = 25\text{ft}^2$, which is why this point is not included.

B. Variation of η_{PR} with A_2 and \dot{m}_2

Fig. 12a shows how η_{PR} , measured at the fan face, varies as a function of the fan annulus area A_2 for a constant \dot{m}_2 requirement. The same data are plotted in Fig. 12b to clearly illustrate how η_{PR} trends with \dot{m}_2 for a fixed A_2 . Solid



(a) η_{PR} variation with A_2 for different \dot{m}_2



(b) η_{PR} variation with \dot{m}_2 for different A_2

Fig. 12 Experiment 1: variation of η_{PR} as a function of A_2 and \dot{m}_2

lines denote trends for η_{PR} measured at the fan face (p_{t2}/p_{t0}), while dashed lines represent trends of η_{PR} measured at a plane slightly offset from the inlet highlight (p_{t1}/p_{t0}), not shown in Fig. 12a). The latter results quantify the airframe contribution to η_{PR} . The difference between the solid and dashed curves indicates the effective contribution of the inlet to η_{PR} .

Like with $C_{PK_{in}}$, pressure recovery shows a positive correlation with A_2 and negative with \dot{m}_2 as hypothesized. Consider the η_{PR} contours shown at the fan face in Fig. 13. Comparing Fig. 13a to c or Fig. 13b to d, it can be seen that the larger propulsor ingests more clean flow at a higher total pressure compared to the smaller propulsor. Additionally, while the extent of the ingested boundary layer is similar for both propulsor sizes, the total pressure variations in the boundary layer are not. For the larger propulsor, the ingested boundary layer has a higher η_{PR} compared to the smaller propulsor for the same \dot{m}_2 . Differences in the captured streamtube, as discussed in relation to the $C_{PK_{in}}$ trends, is one reason for this observation. The larger propulsor essentially ingests flow further away from the wall, from a region of higher total pressure, which in conjunction with ingesting more clean flow, has a favorable impact on η_{PR} and explains the positive correlation with A_2 .

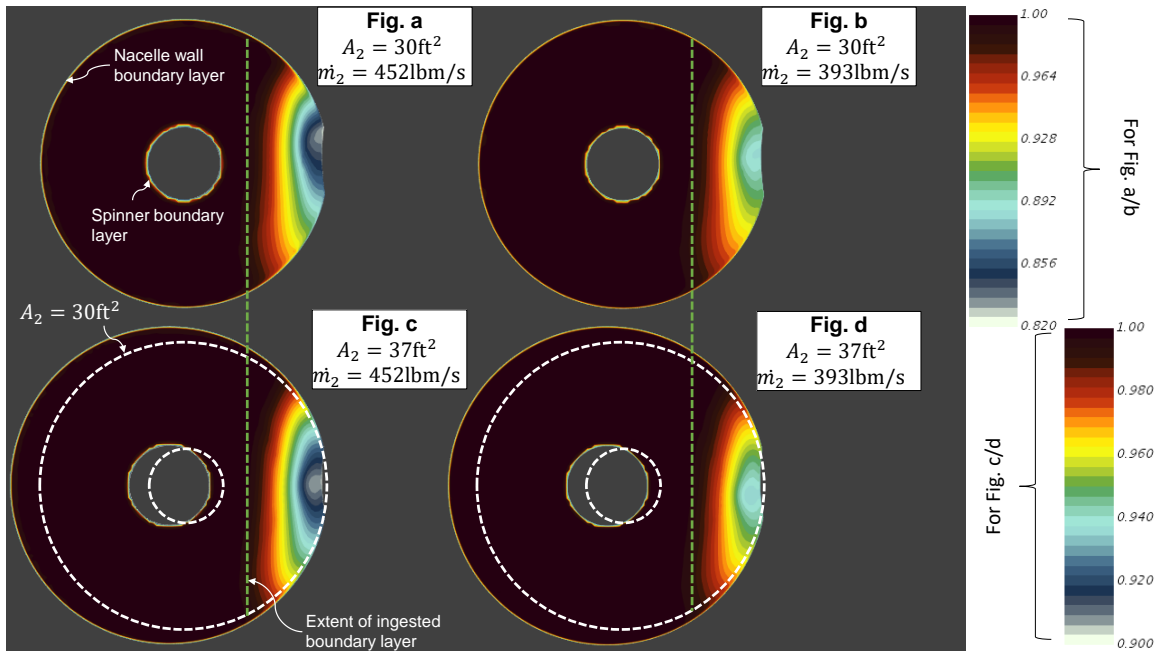
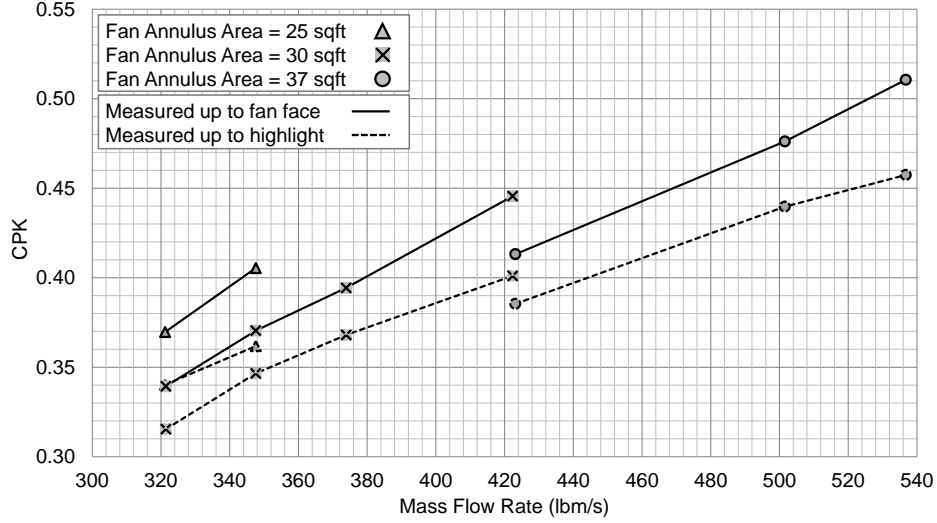


Fig. 13 Experiment 1: η_{PR} contours at the fan face

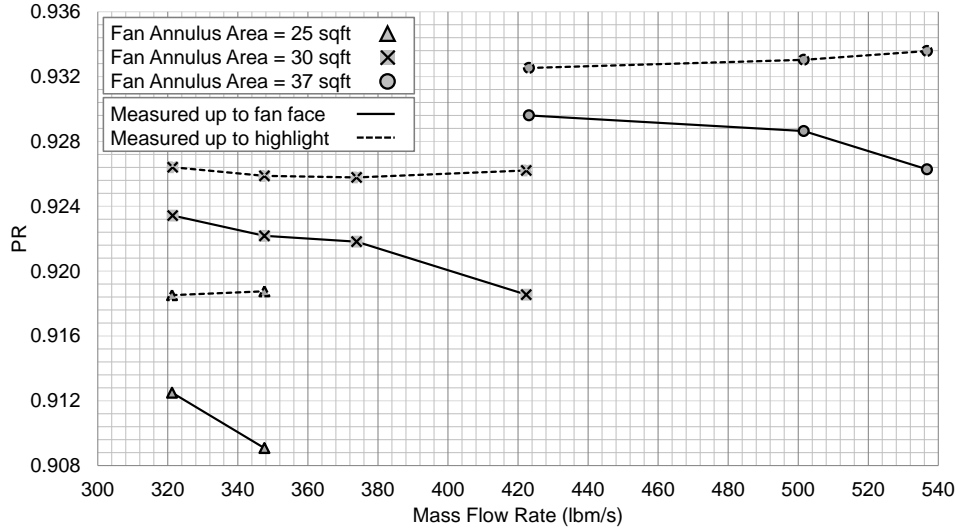
Impacts of the propulsor on the wall shear stress also explain the η_{PR} trends observed. The velocity gradient at the wall, and thus shear stress, is larger for a higher flow rate. Similarly, for a fixed flow rate requirement, decreasing A_2 increases the inflow velocity and wall shear. This increase in viscous losses maps to a decrease in η_{PR} with \dot{m}_2 . The presence of a shock in the inlet for $\dot{m}_2 = 434\text{lbm/s}$ and $\dot{m}_2 = 452\text{lbm/s}$ for the smallest propulsor has a detrimental impact on η_{PR} , unlike with $C_{PK_{in}}$. Thus, $C_{PK_{in}}$ in isolation is not an adequate metric to gage the BLI benefit and η_{PR} must also be considered to assess the net impact on propulsor performance.

VII. Experiment 2: Case B Boundary Layer Ingestion

Fig. 14 shows the $C_{PK_{in}}$ and η_{PR} results as a function of \dot{m}_2 . Unlike previously, $C_{PK_{in}}$ now shows a positive correlation with \dot{m}_2 and negative with A_2 . Additionally, the sensitivity of $C_{PK_{in}}$ to changes in \dot{m}_2 is higher than for the side-engine case. Pressure recovery at the fan face still shows a positive correlation with A_2 and negative with \dot{m}_2 , however, η_{PR} at the highlight trends differently with \dot{m}_2 . To understand these trends, one must understand the relation between $C_{PK_{in}}$ and $\frac{V}{V_{\infty}}$. Fig. 15 compares the $C_{PK_{in}}$ and $\frac{V}{V_{\infty}}$ contours at the fan face of the $A_2 = 30\text{ft}^2$ propulsor for different flow rates. One key observation from these contours is the ‘bucket like’ variation in both $C_{PK_{in}}$ and $\frac{V}{V_{\infty}}$. The contours exhibit a ‘lung’ shaped pattern, not very dissimilar to the total pressure contours observed for the STARC-ABL at low angles of attack in [12]. Within this ‘lung’ shaped sector, the zone of low $\frac{V}{V_{\infty}}$ flow corresponds to a zone of



(a) $C_{PK_{in}}$ variation with \dot{m}_2 for different A_2



(b) η_{PR} variation with \dot{m}_2 for different A_2

Fig. 14 Experiment 2: variation of $C_{PK_{in}}$ and η_{PR} with A_2 and \dot{m}_2

low $C_{PK_{in}}$. Outside this zone, there is a peak in $C_{PK_{in}}$, after which it decreases radially upwards, while $\frac{V}{V_{\infty}}$ increases, transitioning from boundary layer flow to freestream. In other words, these contours highlight the non-monotonic behavior of $C_{PK_{in}}$ with $\frac{V}{V_{\infty}}$, more clearly illustrated in Fig. 16.

In this figure, the integrand of $C_{PK_{in}}$ in Eq. (3) is plotted as a function of $\frac{V}{V_{\infty}}$ at each of the \dot{m}_2 values tested for $A_2 = 30\text{ft}^2$. Unlike Fig. 8, the x axis should not be considered as the average fan face velocity for a given \dot{m}_2 , but rather, a domain of possible velocity ratios that can be seen on the fan annulus for a given flow rate. To generate this figure, an estimate for how the mass flux ρV varies as a function of $\frac{V}{V_{\infty}}$ is obtained by fitting a surrogate to the average mass flux data obtained for all propulsors tested in experiment 2. Note that a given value of \dot{m}_2 corresponds to a fixed value of C_p given the uniform boundary condition imposed at the fan face. Fig. 16 essentially shows how the $C_{PK_{in}}$ integrand varies at different points on the fan annulus where the flow is at different $\frac{V}{V_{\infty}}$. Initially, $C_{PK_{in}}$ increases with velocity, but then the second order effects due to $1 - \frac{V^2}{V_{\infty}^2}$ result in a decrease in $C_{PK_{in}}$ with $\frac{V}{V_{\infty}}$. The optimum value of $\frac{V}{V_{\infty}}$, where the integrand peaks in value, increases with \dot{m}_2 . The trends shown in Fig. 16 mirror the contours shown in Fig. 15.

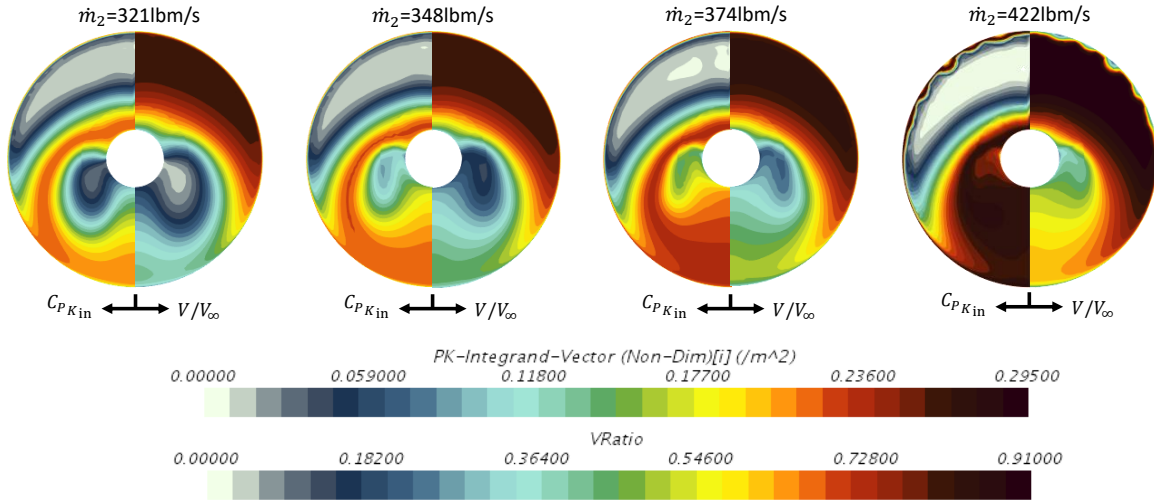


Fig. 15 Experiment 2: contour plots of $C_{P_{K_{in}}}$ and $\frac{V}{V_{\infty}}$ shown at the fan face for $A_2 = 30ft^2$ at different \dot{m}_2

As required \dot{m}_2 increases, the value of the C_{P_2} boundary condition at the fan face decreases. In conjunction with the increase in mass flux in the linear region of the $C_{P_{K_{in}}}$ curve, the net result is an increase in $C_{P_{K_{in}}}$ with \dot{m}_2 . Thus, as hypothesized, the amount of ingested boundary layer does play a role in influencing the sensitivity of $C_{P_{K_{in}}}$ to \dot{m}_2 .

The fan face trends for η_{PR} are consistent with experiment 1, as expected, however, the inlet highlight values show inconsistent trends. This behavior is due to flow separation at the tail cone, as shown in Fig. 17. In this figure, streamlines are shown at the lowest and highest flow rate values for the $A_2 = 30ft^2$ propulsor. The velocity ratio scalar values are shown on the streamlines and at the fan face. For low flow rates, the adverse pressure gradient imposed by the fan and the tapering geometry results in flow separation on the bottom and side of the tail cone. This recirculating flow from both zones mixes into a vortical structure of low velocity and low total pressure, which extends partly into the nacelle, but not up to the fan face. As the flow rate increases, the extent of this recirculating flow region reduces, as seen in Fig. 17. The lung shaped patterns seen in Fig. 15 are due to this flow separation. While the η_{PR} trends with A_2 are consistent with experiment 1, $C_{P_{K_{in}}}$ trends are not. There are two reasons for this behavior. First, for the same mass flow

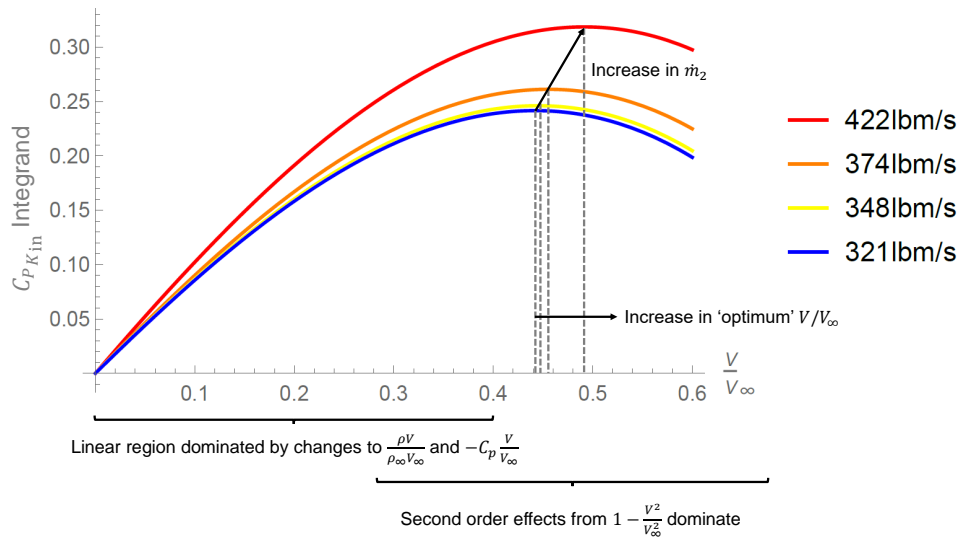


Fig. 16 Experiment 2: plot showing $C_{P_{K_{in}}}$ integrand varying as a function of $\frac{V}{V_{\infty}}$ at different required \dot{m}_2 for $A_2 = 30ft^2$

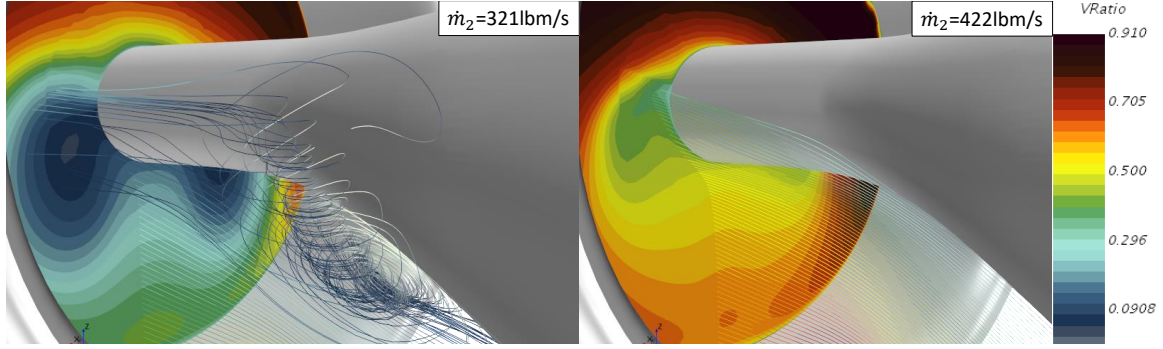


Fig. 17 Experiment 2: flow separation observed at the tail cone, in front of the inlet highlight, for $\dot{m}_2 = 321\text{lbm/s}$, which is virtually eliminated at $\dot{m}_2 = 422\text{lbm/s}$ for $A_2 = 30\text{ft}^2$. Contours of $\frac{V}{V_\infty}$ are shown at the fan face and on the streamlines

rate, the smaller propulsor has a higher ρV . Since a large portion of the fan-face sees low velocity flow, evident in Fig. 15, this region is in the linear domain of the plot shown in Fig. 16. Thus, increases in ρV due to a decrease in A_2 for the same mass flow, for this specific configuration, result in an increase in $C_{P_{K_{in}}}$. Second, the differences also arise from the presence of shocks in the inlet for the highest flow rate. The shocks for the smaller propulsor are stronger than those in the larger propulsor, for the same flow rate. For the inlet highlight results, the larger propulsor tends to induce a larger extent of flow separation at the tail cone, for the same flow rate. Thus, for these three comparison points, $C_{P_{K_{in}}}$ is smaller for a larger A_2 .

VIII. Conclusions

The experiments conducted in this study investigated the trends of the BLI effects with fan size, represented by the fan annulus area, and engine operation, represented by the required mass flow rate. Two sets of experiments were conducted for different engine locations. In experiment 1, the engine was on the side of the fuselage, like on the NOVA-BLI. For experiment 2, the engine was mounted on the aft end, like on the STARC-ABL. These two locations experience different circumferential and radial extents of ingested boundary layer. For each location, a small set of trials was conducted where the fan annulus area was changed for a fixed flow rate requirement, followed by a change in the flow rate, for a fixed fan size. The main findings are summarized below:

- 1) The metric $C_{P_{K_{in}}}$ shows a positive correlation with fan size and negative with flow rate, for a low ingested boundary layer extent and in the absence of inlet shocks
- 2) The same response shows opposite correlations with fan size and flow rate when the extent of the ingested boundary layer is much higher
- 3) The BLI effect η_{PR} shows a positive correlation with fan size and a negative correlation with flow rate, assuming no flow separation
- 4) Presence of inlet shocks have a favorable impact on $C_{P_{K_{in}}}$, with small propulsors showing a positive correlation with flow rate if shocks exist
- 5) Flow separation at the measurement plane on which η_{PR} is being calculated results in η_{PR} showing a positive correlation with flow rate, as long as separation is present and its extent reduces with an increase in flow

It is apparent that the experimental results agree with general physics based reasoning, with the exceptions arising in situations where shocks or flow separation have a direct impact on the measured quantity at a given propulsor station. While the geometries used in these experiments are not optimized for a given flight condition, the presence of shocks or separation for some cases, but not for others, highlights the role played by the propulsor in affecting local flow characteristics. For example, in experiment 1, shocks were observed inside the inlet for the smallest propulsor at the highest flow rates, but not otherwise. This suggests that the nacelle contouring may not have been a big factor and that perhaps the fan diameter was too small for the required flow rates. Increasing the fan diameter for the same flow rates and nacelle design eliminated these shocks. However, if most of the cases in experiment 1 showed inlet shocks, then such a scenario would have been indicative of a poor inlet design, requiring more detailed design refinement. The underlying theme is the same as that studied in [4], i.e., there are macro parameters that are primarily responsible for major changes to the flow (A_2 and \dot{m}_2), and that the detailed parameters (inlet contouring) have a relatively smaller

impact as long as these parameters are set to reasonable values that do not result in adverse flow for most cases. Note, this point does not imply that the detailed nacelle contouring is irrelevant. Merely, for conceptual design purposes, fan size and flow rate play a much bigger role. Thus, refinement of the inlet contours can be conducted in preliminary design. Similarly, the flow separation observed in experiments 1 and 2 for low flow rate cases can be mitigated by altering airframe macro parameters like the angle of the fuselage entering the propulsor for experiment 1 and tail cone upsweep angle for experiment 2. While shocks and flow separation are likely at corner points within a design space, these points will be filtered out at the system level design if these features have a net negative impact on performance.

With respect to the aero-propulsive coupling methodology for BLI concepts, the experiments conducted in this study show the significance of propulsor on-design and off-design impacts on the ingested inflow and thus on the value of the BLI effects. For a parametric methodology, both A_2 and \dot{m}_2 , or equivalent quantities capturing fan size and operation impacts, need to be part of the input space. The trends investigated in this paper can be used to explain system level impacts of BLI on fuel burn.

References

- [1] Gray, J. S., Mader, C. A., Kenway, G. K., and Martins, J. R. R. A., "Modeling Boundary Layer Ingestion Using a Coupled Aeropropulsive Analysis," *Journal of Aircraft*, Vol. 55, No. 3, 2018. <https://doi.org/10.2514/1.C034601>.
- [2] Gray, J. S., and Martins, J. R. R. A., "Coupled Aeropropulsive Design Optimization of a Boundary Layer Ingestion Propulsor," *The Aeronautical Journal*, 2018, p. 19.
- [3] Rodriguez, D. L., "Multidisciplinary Optimization Method for Designing Boundary-Layer-Ingesting Inlets," *Journal of Aircraft*, Vol. 46, No. 3, 2009. <https://doi.org/10.2514/1.38755>.
- [4] Ahuja, J., and Mavris, D. N., "Sensitivity of Boundary Layer Ingestion Effects to Tube and Wing Airframe Design Features," *AIAA SciTech Forum*, AIAA, 2020.
- [5] Pokhrel, M., Shi, M., Ahuja, J., Gladin, J. C., and Mavris, D. N., "Conceptual Design of a BLI Propulsor Capturing Aero-Propulsive Coupling and Distortion Impacts," *AIAA SciTech Forum*, AIAA, 2019.
- [6] Ahuja, J., and Mavris, D. N., "A Method for Modeling the Aero-Propulsive Coupling Characteristics of BLI Aircraft in Conceptual Design," *AIAA SciTech Forum*, AIAA, 2021.
- [7] Drela, M., "Power Balance in Aerodynamic Flows," *AIAA Journal*, Vol. 47, No. 7, 2009.
- [8] Hall, D. K., Huang, A. C., Uranga, A., Greitzer, E. M., Drela, M., and Sato, S., "Boundary Layer Ingestion Propulsion Benefit for Transport Aircraft," *Journal of Propulsion and Power*, Vol. 33, No. 5, 2017.
- [9] Wiart, L., Atinault, O., Grenon, R., Paluch, B., and Hue, D., "Development of NOVA Aircraft Configurations for Large Engine Integration Studies," *33rd AIAA Applied Aerodynamics Conference*, AIAA, 2015.
- [10] Lord, W. K., Suci, G. L., Hasel, K. L., and Chandler, J. M., "Engine Architecture for High Efficiency at Small Core Size," *AIAA SciTech Forum*, AIAA, 2015.
- [11] Welstead, J. R., and Felder, J. L., "Conceptual Design of a Single-Aisle Turboelectric Commercial Transport with Fuselage Boundary Layer Ingestion," *AIAA SciTech Forum*, AIAA, 2016. <https://doi.org/10.2514/6.2016-1027>.
- [12] Kenway, G. K., and Kiris, C., "Aerodynamic Shape Optimization of the STARC-ABL Concept for Minimal Inlet Distortion," *AIAA SciTech Forum*, AIAA, 2018. <https://doi.org/10.2514/6.2018-1912>.